Geophys. J. Int. (2009) **179,** 549–558 doi: 10.1111/j.1365-246X.2009.04262.x

InSAR observations of 2007 Tanzania rifting episode reveal mixed fault and dyke extension in an immature continental rift

Juliet Biggs,[1] Falk Amelung,[1] Noel Gourmelen,[1] Timothy H. Dixon[1] and Sang-Wan Kim[2]

[1]*Rosenstiel School of Marine and Atmospheric Sciences, University of Miami, Miami, FL, USA. E-mail: jbiggs@rsmas.miami.edu*
[2]*Department of Geoinformation Engineering, Sejong University, Seoul, Korea*

Accepted 2009 May 20. Received 2009 May 20; in original form 2008 September 24

SUMMARY

In the early stages of continental rifting, extension takes place by normal faulting, while in mature continental rifts dyke intrusion dominates. Little is known about the nature of the transition between fault-controlled and dyke-controlled extension or about the processes in an intermediate setting. Here, we present observations of the temporal and spatial evolution of surface displacements during the 2007 July 14–August 4 rifting episode in Northern Tanzania, an immature section of the East African Rift. The ground deformation initiated with subsidence that can be attributed to ∼40 cm of normal motion on a NE striking fault. Following July 17, deformation was dominated by the intrusion of ∼7-km-long dyke. Dyke opening increased gradually to a total of ∼2.4 m. From July 21, the collapse of a shallow graben above the fault dominated the near-field displacements. Comparison to the 2007 Dabbahu dyke, Afar, which occurred in a more mature rift, shows an order-of-magnitude scale difference in dyke length. Using numerical models of dyke propagation, we attribute this to the size and depth of the magma chamber; in immature rifts the thick crust and slow spreading rate favour small, deep magma chambers, forming short, buried dykes, whereas in mature rifts the thinner crust and faster spreading rate favour large, shallow magma chambers and long, erupting dykes. Observing the pattern of active processes in the East African Rift is key to understanding the development of rift systems and passive margins elsewhere.

Key words: Satellite geodesy; Radar interferometry; Continental margins: divergent; Physics of magma and magma bodies; Africa.

1 INTRODUCTION

Most models of continental rifting focus on the fault-controlled aspects of extension. However, recent observations of active extension (Wright *et al.* 2006) have shown patterns of surface displacements that cannot be explained by motion on faults alone. Magma-driven process such as dyke intrusion play an important role, especially in the later stages of rift evolution.

In this paper, we study the time-dependent deformation during the 2007 rifting episode in Tanzania. In Section 2, we use Interferometric Synthetic Aperture Radar (InSAR) to measure the spatial and temporal evolution of the ground displacements and relate these to simple elastic models of subsurface features. We interpret the observations on two different scales. In Section 3, we consider the implications of our observations for the temporal evolution of dyke intrusion episodes and the partitioning of magma- and fault-based extension in an intermediate rift setting. In Section 4, we consider the variation in dyke dimensions along the East African Rift, by comparison with the 2005 Dabbahu Rifting Episode in Ethiopia. We investigate the suggestion that systematic variations in key geophysical parameters associated with the evolution of a continental rift controls the length of dykes in extensional settings. A model of magma-driven dyke propagation can explain these differences in terms of magma chamber size and depth, consistent with changes in the maturity of the rift. We provide a simple hypothesis to be tested by future observations.

1.1 Evolution of East African rift

East Africa is an ideal place to study the development of continental rifting—observing the active processes here is key to understanding rift systems elsewhere (Fig. 1). The East African Rift, separating the Nubian and Somalian Plates, has propagated from north to south, leaving a geographical record of rift development and a systematic variation in geophysical, geochemical and geomorphological properties (Ebinger 2005). As extension increases, the lithosphere thins and spreading rate and melt supply increase. The spreading rate is <1 mm yr^{-1} in the south and reaches $\sim$7 mm yr^{-1} in the north (Sella *et al.* 2002; Stamps *et al.* 2008). Ebinger & Casey (2001) identify three distinct stages of rift formation.

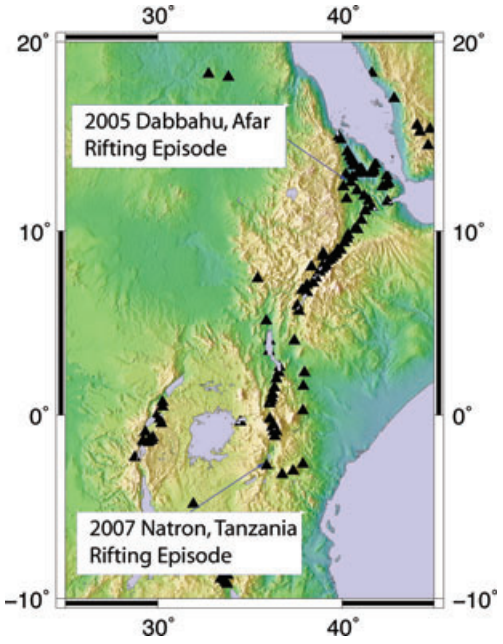

Figure 1. The African Rift Valley extends southward from Afar, as indicated by the active volcanoes (black triangles). The recent seismic swarm occurred at the southern end of the Eastern Rift valley in Tanzania.

(i) *Immature Continental Rift:* Lithospheric thinning through brittle/ductile extension, with major slip along large offset border faults and minor decompression melting (e.g. Tanzania).

(ii) *Mature Continental Rift:* Asthenospheric upwelling leading to increasing melting. Strain localizes into magmatic segments; narrow zones of magmatic intrusions parallel to the earlier faults (e.g. Main Ethiopian Rift).

(iii) *Mid Ocean Ridge:* The thinned lithosphere ruptures along the intruded zone and new oceanic lithosphere is created (e.g. Red Sea Spreading Centre).

Structural observations reveal that the mechanism of extension changes from dominantly fault-based to dominantly magma-based as the rift matures. Towards the south of the East African Rift, where the rifting is younger, extension is accommodated by faulting, and in the northern sections, which are older, extension is accommodated by magmatic processes (Ebinger 2005). The nature and timing of the transition is poorly understood.

1.2 Northern Tanzania

In Northern Tanzania, the Eastern Branch of the Rift Valley splits into a 200-km-wide zone comprised of three distinct rifts with different orientations: the Eyasi-Wembere rift, the Natron-Manyara-Balangida rift and the Pangani rifts (Foster 1997). The topographic graben is asymmetric, bounded to the west by the major Manyara-Natron fault, which forms the rift escarpment (Fig. 2). The rift valley contains a number of volcanoes: Gelai (Figs 1 and 2), is a shield volcano formed during an earlier phase of tectonic activity (Foster 1997). Oldonyo Lengai (Fig. 2) is the only active volcano in the world that produces low temperature, low viscosity natro-carbonitite lavas. Oldonyo Lengai has been intermittently active since 1983, with small scale events within the summit cone (Nyamweru 1990; Dawson *et al.* 1994. 1995; Nyamweru 1997; Kervyn *et al.* 2008). Silica-rich eruptions are typically more explosive (VEI 3) and have occurred three times (1917, 1940–1941, 1966–1967) during the 20th century (Dawson *et al.* 1968).

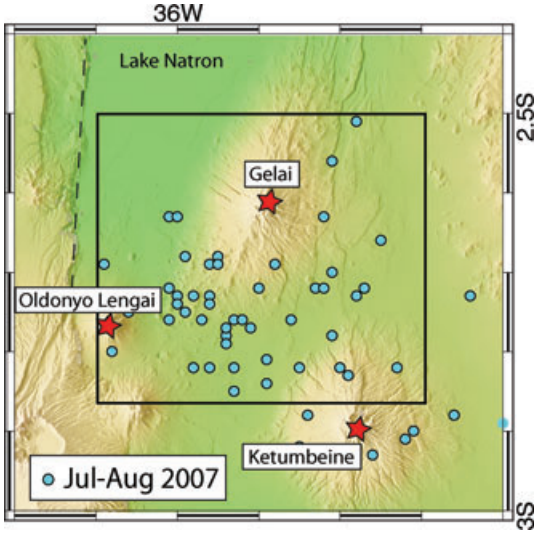

Figure 2. Location of the 2007 Lake Natron Seismic Swarm. Dots represent earthquake locations from NEIC PDE catalogue. Stars mark the nearby volcanoes: Oldonyo Lengai, Gelai and Ketumbeine. The black box marks the location of Fig. 4

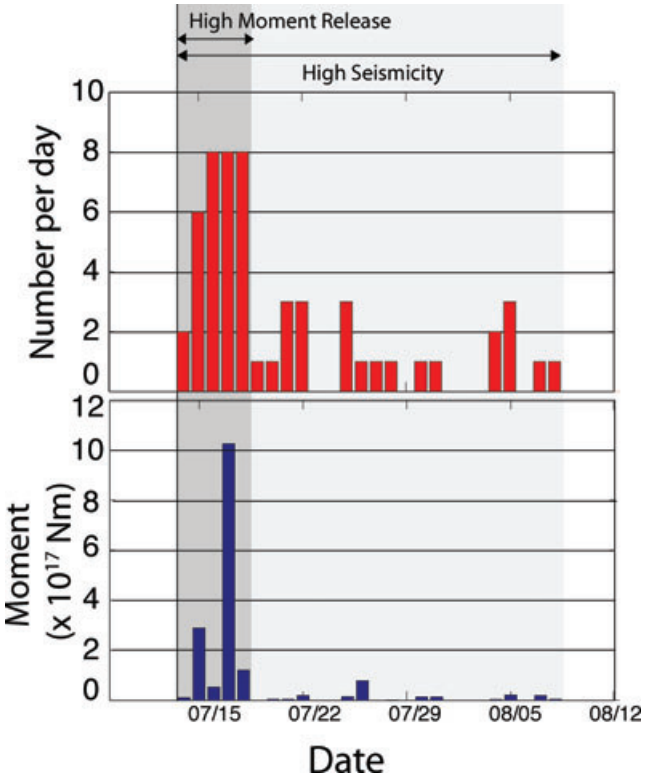

Figure 3. Seismicity during the 2007 Lake Natron Seismic Swarm. Daily earthquake numbers and moment through time as recorded by the NEIC PDE catalogue. The swarm lasted for 22 d, but the majority of the moment was released during the first 5 d.

1.3 The 2007 Natron, Tanzania rifting episode

From 2007 July 14 to August 4, a swarm of 57 moderate-sized earthquakes (m_b3.6–5.9) was recorded in Northern Tanzania (Fig. 2). We use the NEIC PDE catalogue to calculate the number of earthquakes and moment release for each day of the swarm (Fig. 3). Events for

which the body wave magnitudes are given are converted to moment magnitudes using the empirical global relationship of Scordilis (2006), then the moment of each event is calculated using the relationship of Kanamori (1977). Using 356 earthquake recorded during the past 20 yr in eastern Africa, we estimate the completeness of this catalogue to be $\sim m_b 4.2$. A temporary local network was located just to the south of the Natron basin at this time and recorded a total of 607 earthquakes aligned along a steeply dipping plane striking N33E (Calais *et al.* 2008). The seismic moment release was greatest during the first 5 d, dominated by a M5.9 earthquake on July 17th (Fig. 3). Six earthquakes with $M_w > 5.0$ appear in the Global CMT catalogue (Dziewonski & Anderson 1981) with normal faulting mechanisms with dips in the range 45–60° and strikes of 50–70°.

Satellite-based spectral emissivity measurements show a hotspot at the summit of the nearby Oldonyo Lengai Volcano in mid-June with temperatures of 440 °C (consistent with on-going natrocarbonitite activity) and an increase in temperature to 550 °C on September 4 (consistent with a shift to a more silica-rich composition) (Vaughan *et al.* 2008). Field observations show metre to kilometre long tension fractures on the southern flank of Gelai forming a central graben 2–3 km wide oriented NNE–SSW (Calais *et al.* 2008; Baer *et al.* 2008). Estimates of the vertical offsets are up to 12 cm (Calais *et al.* 2008) or 50 cm (Baer *et al.* 2008). Local inhabitants report initial cracking with vertical offsets of a few centimetres followed by gradual subsidence accompanied by the formation of new cracks (Baer *et al.* 2008).

2 GEODETIC OBSERVATIONS AND ELASTIC MODELLING

2.1 InSAR observations

Radar acquisitions by the satellites Envisat (ESA) and ALOS (JAXA) permit us to create five interferograms, dense maps of ground displacement, spanning several discrete periods of the rifting episode (Table 1). The interferograms were processed using the ROIPAC software (Rosen *et al.* 2004) and unwrapped using a branch cut algorithm (Goldstein *et al.* 1988). The topographic effects were removed using a 90 m DEM provided by the Shuttle Radar Topography Mission (SRTM). The interferograms are all taken from the same direction (ascending passes) but have a range of incidence angles, making direct comparison between images impossible.

The interferograms show no movement around the summit of Oldonyo Lengai but complex ground deformation on the southern flank of the inactive volcano, Gelai. The peak radar line-of-sight displacement (42 cm) is larger than expected for a shallow *M*5.9 earthquake, indicating significant aseismic motion. Despite the difference in look angle, the displacement patterns are clearly inconsistent between interferograms, requiring different deformation sources during different time periods.

Table 1. Interferograms used in this study.

Satellite	Look angle	Start date	End date	$B_\perp$(m)
Envisat	40°	April 03	July 17	59
ALOS	41°	June 05	July 21	541
Envisat	23°	March 05	July 23	287
Envisat	40°	July 17	August 21	118
Envisat	23°	July 23	August 27	29
Radarsat	40°	2001 August 31	2004 August 15	216

Notes: All dates are from 2007 unless otherwise stated. $B_\perp$ is the perpendicular baseline of the interferogram.

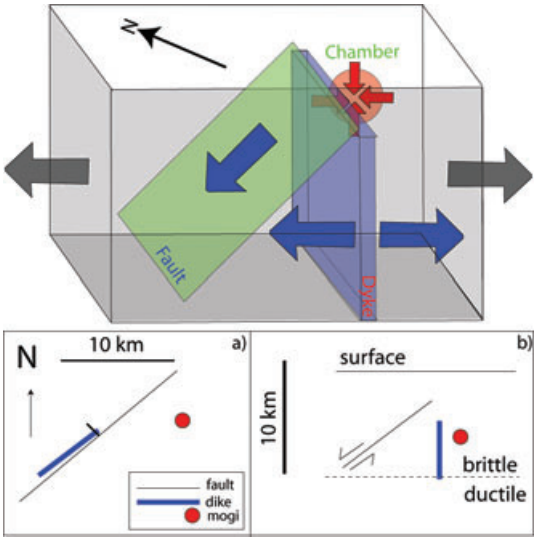

Figure 4. Geometry of subsurface features active during the 2007 Lake Natron Swarm. Cartoon is not to scale and is intended to aid visualization only. (a) plan view (b) cross-section.

2.2 Elastic modelling of geodetic observations

Each interferogram is modelled independently but the sources are based on common features (1 fault, 1 dyke and 1 magma chamber) compatible with multiple interferograms (Figs 4 and 5). We identify an additional source, a shallow graben, but for modelling purposes we mask this out and discuss it in more detail in a subsequent section. This approach is different from that of Baer *et al.* (2008) and Calais *et al.* (2008) who fix the geometry of their models using surface fissures. However, the upper 1–2 km of the crust does not behave as an elastic half-space and the geometry of the numerous subparallel fissure strands is affected by pre-existing structures or local heterogeneities in bulk properties. We chose to focus instead on the deeper processes that are the primary focus of this paper. Our simpler three-source geometry uses comparatively few model parameters but still fits the changing patterns of deformation observed in the full range of interferograms. In particular, the model does not require an additional mogi source under the Natron Basin as suggested by Calais *et al.* (2008) or a second dyke as suggested by Baer *et al.* (2008) despite using uniform rather then distributed opening and slip.

Elastic modelling is carried out using the matlab-based geodmod software developed at the University of Miami. Forward models for fault slip and dyke opening are calculated using the Okada formulation for motion on a uniform rectangular dislocation in a homogeneous, elastic half-space (Okada 1985), and for the magma chamber using the Mogi formulation for inflation of a point source (Mogi 1958). The interferograms are subsampled using either a uniform grid or quadtree algorithm (Jonsson *et al.* 2002) as appropriate. The source geometry is inferred using a non-linear Monte-Carlo type inversion procedure (Cervelli *et al.* 2002) and the source strengths by linear inversion. Due to trade-offs between multiple sources, we reduce the number of free parameters by manually selecting relevant source elements and fixing parameters wherever possible (Table 2).

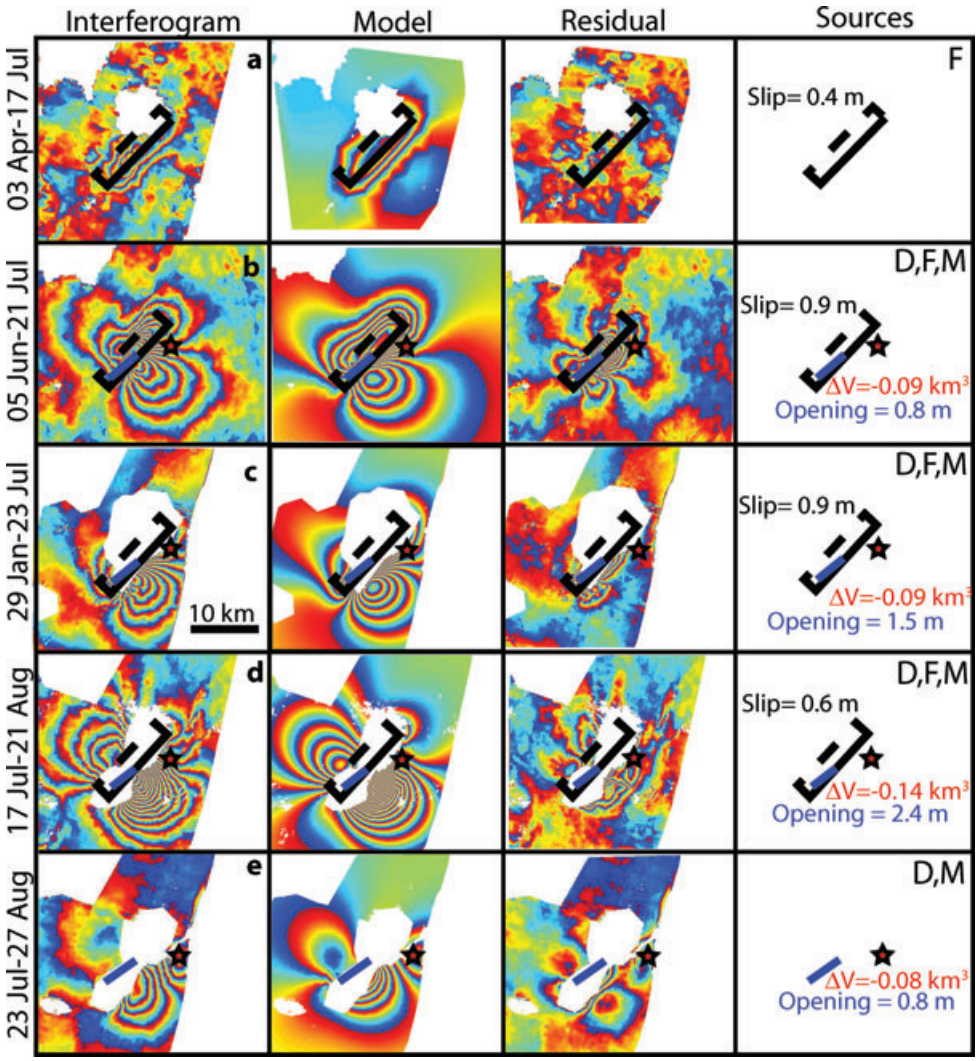

Figure 5. Matrix of interferograms, models and residuals for various time periods of the 2007 Lake Natron rifting episode. Model elements are made up of a dyke (D), a fault (F) and a Mogi source (M) indicated in the top right corner of the source column. Each fringe represents a line-of-sight displacement of 2.8 cm (NB: The ALOS interferogram has been re-wrapped to match the Envisat wavelength). The strength of each source (opening, slip and deflation respectively) vary according to the time period. All figures are at the same scale (see scale bar in interferogram c) and the extents are shown in Fig. 2. The axial collapse zone is masked out (see Section 2.5). The images are interpolated from the subsampled data, resulting in a blocky appearance in some cases.

2.3 Detailed observations and elastic modelling

2.3.1 03 April–17 July (Fig. 5a)

This interferogram covers the first 3 d of the seismic swarm only and shows an elongated pattern of three concentric fringes. This pattern is typical of a normal faulting earthquake. Elastic models show ∼40 cm of slip along a ∼16-km-long buried fault dipping to the NW. This simple model fits the data very well, and the residual is low.

2.3.2 05 June–21 July (Fig. 5b)

This interferogram covers the first 7 d of the seismic swarm and the fringe pattern is more complex than that in the previous interferogram. The concentric fringes associated with normal faulting are still present, but superimposed on this are two lobes of fringes, in a pattern typically associated with dyke opening. Elastic models show ∼90 cm of slip along the fault, and ∼80 cm of opening along a subparallel dyke ∼7 km in length. The presence of a mogi source is inferred from a later interferogram and found to significantly reduce the model misfit to this and all subsequent interferograms. This model fits the far-field displacement pattern, but there is a large residual located immediately above the dyke. The residual is mainly confined to the location of the shallow graben seen in later interfeograms (Figs 5c–d). Although the major graben-bounding fissures have yet to form in this time period (Section 2.5), there has been a significant amount of dyke opening and we attribute the residual to subsidence above the dyke. Furthermore, the near-field displacements pattern is sensitive to complexities in geometry and opening, which are over-simplified by our single-plane uniform slip model, typically resulting in a large but localized misfit.

2.3.3 29 January–23 July (Fig. 5c)

This interferogram covers the first 9 d of the seismic swarm and the far field fringe pattern is very similar to that of the previous interferogram. However, the axial zone now shows a high fringe gradient, associated with the collapse of a shallow graben (masked out of the figure). Elastic modelling uses the same elements as the

Table 2. Model parameters for the 2007 Lake Natron Intrusion.

Source	X	Y	Depth	Length	Width	Strike	Dip	Mag	Moment
April 03–July 17; Envisat IS6; rms = 12.3 mm									
Fault	36.081	2.696	3.6	16.1	5.2	43	53	0.42	1.1
June 05–July 21; Envisat IS2; rms = 51.0 mm									
Fault	36.081∗	2.696∗	3.6∗	16.1∗	5.2∗	43∗	53∗	0.92	2.3
Dyke	36.052	2.716	4.1	7.0	3.6	47	90∗	0.79	0.6
Mogi	36.13∗	2.68∗	5.6∗					8.9	
January 29–July 23; ALOS; rms = 22.7 mm									
Fault	36.081∗	2.696∗	3.6∗	16.1∗	5.2∗	43∗	53∗	0.92	2.3
Dyke	36.052	2.716	4.4	6.3	3.1	49	90∗	1.5	0.9
Mogi	36.13∗	2.68∗	5.6∗					8.9	
July 17–August 23; Envisat IS6; rms = 20.2 mm									
Fault	36.081∗	2.696∗	3.6∗	16.1∗	5.2∗	43∗	53∗	0.55	1.4
Dyke	36.055	2.717	4.3	7.2	3.3	48	90∗	2.41	1.7
Mogi	36.13∗	2.68∗	5.6∗					13.7	
July 23–August 27; Envisat IS2; rms = 15.2 mm									
Dyke	36.047	2.710	4.0	7.6	4.3	55	90∗	0.8	0.8
Mogi	36.15	2.68	5.0					7.8	

Notes: Asterisks indicate parameters fixed from alternative interferograms to reduce trade-offs.

previous interferogram, but required additional opening on the dyke of ∼70 cm during July 22–23; making a total of ∼1.5 m for this interferogram.

2.3.4 17 July–21 August (Fig. 5d)

This interferogram begins on the fourth day of the seismic swarm and includes the majority of observed deformation, excluding only the normal faulting observed in the first interferogram. Elastic modelling shows ∼40 cm of slip occurred on the normal fault, with a total dyke opening of ∼2.4 m.

2.3.5 23 July–27 August (Fig. 5e)

This interferogram begins on the 10th day of the seismic swarm and covers the final period. The fringe pattern shows a single lobe of dyke opening, and a concentric fringe pattern located to the NE, typical of a deflating magmatic source. The location of the deflating mogi source is fixed by the surface fringes and we find a depth of 4–8 km. The depth is poorly constrained due to trade-offs with source strength.

2.4 Summary

The earliest interferogram (ending on July 17) shows an elongated pattern of concentric fringes consistent with a normal-faulting earthquake (Fig. 5a). Following July 17, all interferograms show two lobes of deformation consistent with dyke opening (Figs 5b–e). Following July 21, the interferograms show a zone with a high north–south fringe gradient, consistent with the collapse of a near-surface graben (Figs 5c–e). Note that the sense of displacement for both the dyke and the normal fault are consistent with extension (least horizontal principal stress) orientated NW–SE.

2.5 Moment release

We calculate the geodetic moment on the dyke and fault for each time period and compare it to the seismic moment for the same time period (Table 2). Geodetic moment for dyke opening is obtained by taking the product of fault area, amount of opening and shear modulus (30 GPa). Seismic moment is calculated from the NEIC PDE catalogue as described in Section 1.3.

During the first 3 d of the episode (to July 17), the geodetic moment on the fault (1.1×10^{18} N m) is a factor of two larger than the seismic moment (0.47×10^{18} N m). This is consistent with the suggestion that some of the slip occurred aseismically (Calais *et al.* 2008), but our findings do not support an order of magnitude difference. For the interferograms ending on the July 21 and July 23, the geodetic moment associated with the fault slip exceeds the seismic moment by a similar absolute amount ($3–5 \times 10^{17}$ N m). For the final two interferograms, starting on July 17 and July 23, the dyke opening dominates the combined geodetic moment, and the seismic moment is larger than the geodetic moment associated with fault slip. This is clearly illustrated by the interferogram starting on July 23 for which no fault slip is observed, but for which the seismic moment is 7.2×10^{17} N m. The earthquakes during this time were numerous but small and associated with the continuing dyke opening.

The cumulative moment release associated with the teleseismically recorded earthquakes is 1.5×10^{18} N m. This is consistent with the 2.3×10^{18} N m attributed to motion of the fault in our geodetically based model. The division between the dyke-based and fault-based moment release is roughly equal (the geodetically determined moment associated with dyke opening is 1.7×10^{18} Nm). In contrast, moment release during the 2005 Dabbahu, Afar rifting episode was dominated by dyke opening—the geodetically calculated moment associated with dyke opening was an order of magnitude larger than that recorded seismically, and there was no indication of aseismic fault slip (Wright *et al.* 2006). This is broadly consistent with an increase in the proportion of magma-driven extension as the rift matures.

2.6 Shallow graben

Inspection of the raw topography-corrected interferograms shows several interferograms to have a complex displacement pattern of up to ∼50 cm in the line-of-sight along an axial zone trending NE–SW (Fig. 6). Also present are several discontinuities and narrow linear bands of decorrelation. A Multi-Aperture Interferogram (MAI; Bechor & Zebker 2006) constructed using the method of Jung *et al.* (2009) measures horizontal displacements in the along-track direction (Fig. 7). The most notable feature is 30–40 cm of southward directed motion which matches both the pattern and location of

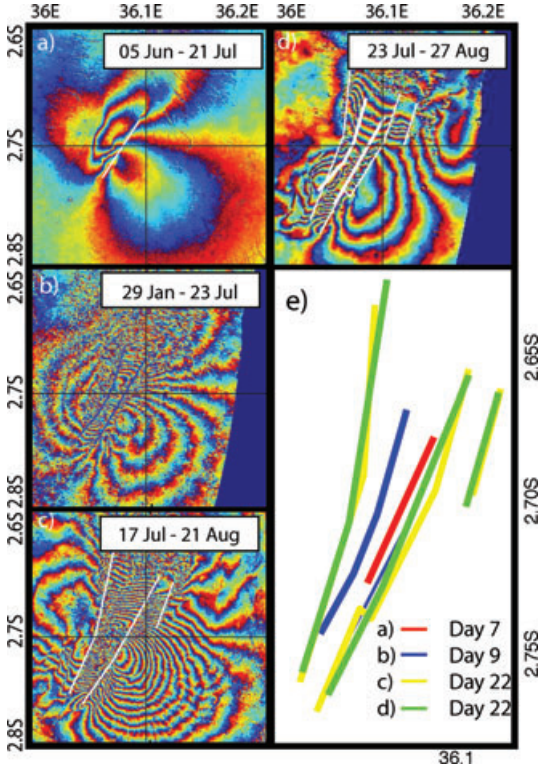

Figure 6. Unfiltered, wrapped interferograms for the 2007 Lake Natron Intrusion showing the surface discontinuities and the extent of the near-surface collapse zone.(a) June 05–July 21 (b) January 29–July 23 (c) July 17–August 21 (d) July 23–August 27 (e) map view of extent of the collapse zone during different time periods (mapped from the interferograms). The collapse zone increases in both length and width with time. Interferograms are displayed as unconverted phase change: for ALOS (a), each fringe represents 11 cm of line-of-sight displacement and for Envisat (b–d) each fringe represents 2.8 cm of line-of-sight displacement. No collapse zone is visible in the interferogram April 3–July 17.

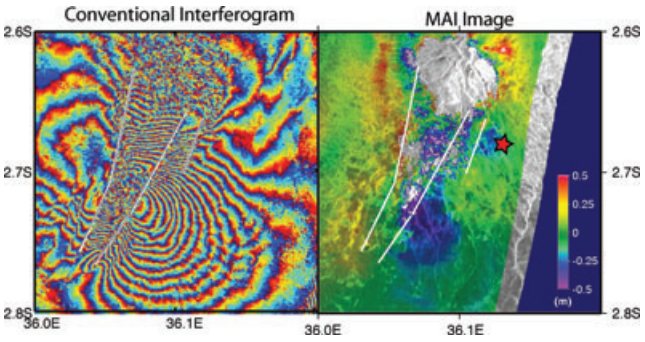

Figure 7. Interferogram for the period July 17–August 21 processed using both conventional and Multi-Aperture (MAI) intererometry techniques. The conventional interferogram measures displacement in the satellite line of sight, in this case 40° to the vertical. Each fringe represents 2.8 cm of displacement. The MAI image measures horizontal displacement in the along-track direction, with an estimated error of ∼5 cm. The axial zone is bounded by the white lines. The conventional interferogram shows 18–20 fringes (∼50 cm) in this area, but the MAI image shows no systematic displacement pattern associated with this feature. Together these images indicate the motion in the axial zone is mostly vertical, consistent with the rapid subsidence of a shallow graben.

the fringes east of the dyke. There are no systematic displacements associated with the axial zone (bounded by the white lines). The measurement error is estimated to be ∼5 cm. This indicates that the motion within the axial zone seen in the interferogram (18–20 fringes) is mostly vertical with little or no horizontal component.

The axial features are attributed to rapid subsidence created by a near surface collapse zone. Mapping the extent of the collapse shows its width to increase with time, and dyke opening (Fig. 6e). Collapse zones are commonly observed above dyke intrusions (Rubin 1992; Wright *et al.* 2006; Rowland *et al.* 2007) and the observations of a number of ground cracks and faults (Baer *et al.* 2008; Calais *et al.* 2008) supports this interpretation. While these features dominate the surface displacements in the axial region, their relative displacements cannot be connected to the far-field due to unwrapping restrictions. Since they neither affect, nor inform us of the deeper source processes in which we are particularly interested, we chose to mask the collapse features from the interferograms in the subsequent analyses. However, we note that the general orientation of the collapse structure is also consistent with NW–SE extension.

3 IMPLICATIONS FOR EVOLUTION OF RIFTING EPISODES

In the previous section, we described the motion on four separate elements which were active during the Tanzania rifting episode: the fault, the dyke, the magma chamber and the shallow graben. In this section, we discuss the implications of these observations for the development of individual rifting episodes.

3.1 Episode initiation

Seismic swarms are frequently associated with dyke intrusions but often it is not possible to determine whether the sequence initiated with seismic or magmatic activity (Aoki *et al.* 1999; Wright *et al.* 2006). In the Natron event, shallow dyke intrusion did not begin until >3 d after the seismic swarm. The first measurable surface displacement was caused by fault slip suggesting the episode was triggered by a tectonic earthquake. However, it is possible that magma movement at depth produced sufficient stress changes to trigger an earthquake, but insufficient surface displacement to be measurable (Baer *et al.* 2008). In contrast, observations from the Krafla, Iceland dyke show that fissure opening, which initiated on 1975 December 20, triggered a M_s6.5 earthquake, on 1976 January 13 (Buck *et al.* 2006). If the region is in a critical state, any event that causes a suitable perturbation to the stress field, regardless of its nature, can induce both seismic and magmatic activity (e.g. Manga & Brodsky 2006; Walter & Amelung 2007).

3.2 Propagation rates

The duration of emplacement can range from hours to months and may depend on magma viscosity. Activity may also migrate spatially. In the Natron dyke, opening is seen in two independent time periods. The modelled dykes have similar extents suggesting that lateral migration took place on a timescale shorter than the temporal spacing between observations. This is consistent with either a series of subparallel dykes or a single dyke opening widthwise. Previous events have shown that seismic activity and fissure opening migrate laterally, with typical rates of 0.01–10 m s^{-1} (Hauksson 1983; Dziak *et al.* 1995; Rubin 1995). On a longer timescale, daily GPS shows dyke-widening but little lateral migration (Aoki *et al.* 1999). Our observations support a model in which lateral

propagation (recorded by seismicity) takes place in the first 4–6 hr followed by several days or weeks of widening (recorded geodetically).

3.3 Repeated fault slip

Field observations of the fault scarps associated with the Dabbahu dyke in Afar do not follow expected fault-scaling relationships leading to the suggestion that slip on near-surface faults accumulates incrementally or aseismically during dyke emplacement (Rowland *et al.* 2007). We see a similar phenomenon on the shallow, graben-bounding faults here. The dyke intrusion began before July 21 but graben subsidence initiated sometime in the period July 21–23 indicating a time delay between dyke-related subsidence and graben formation. The fault-scaling relationships for the larger events lie within the ranges typical for tectonic earthquakes. Repeated slip on a single fault within days–weeks is inconsistent with a tectonically driven model of the earthquake cycle where strain accumulates at a relatively slow rate. Magma movement is one of a number of processes capable of inducing rapid changes in the stress field, which could be responsible for the repeated slip.

3.4 Relationship to volcanic activity

Despite signs of magmatic activity at Oldonyo Lengai during and after the rifting episode, no significant surface displacement was visible in our interferograms [or in a 3-yr Radarsat-1 interferogram spanning 2001–2004 (Table 1)]. The lack of surface displacement implies that there were no major pressure changes in the shallow magma plumbing system during this time. Either magma was sourced from a deep reservoir and moved rapidly through the shallow system, or the volume change was balanced by magma or gas influx. The pulse of more silicic activity at Oldonyo Lengai beginning in September occurred after the end of the dyke intrusion, and is a clear indication of a plentiful magma supply within the crust.

4 CONTINENTAL-SCALE IMPLICATIONS FOR DYKE PROPAGATION

In this section, we seek to place our observations of the 2007 Natron Rifting Episode into a wider tectonic context. Since the beginning of the satellite geodetic era, two dyke intrusion events have been observed in East Africa. The first was the 2005 Dabbahu rifting episode in Afar, Ethiopia and the second is reported here (Fig. 1). Details of the Dabbahu event are given in a series of papers (Ayele *et al.* 2007; Wright *et al.* 2006; Rowland *et al.* 2007; Ebinger *et al.* 2008; Hamling *et al.* 2009; Keir *et al.* 2009). We note an order-of-magnitude difference in dyke length between the <10-km-long dyke reported here and the 60-km-long Dabbahu dyke in Afar in 2005 (Wright *et al.* 2006). These rifting events occurred in the same overall tectonic setting (i.e. a continental rift), but at different stages of rift maturation.

Dyke propagation models are capable of explaining the differences in dyke length according to differences in the size and depth of magma chambers consistent with the increases in magma flux, spreading rate and cumulative extension associated with rift maturation. Two case studies are insufficient to draw conclusions about the regional distribution of dyke geometries—we provide a hypothesis which can be tested by future dyke intrusion episodes in East Africa, and if necessary refined. Other examples from the Asal-Ghoubbet Rift in Djibouti and Northern Iceland are discussed in Section 4.3.

A single magma chamber is capable of feeding a sequence of dykes of varying length, as illustrated by the 1975–1986 dyke intrusion sequence in Krafla, Iceland (Buck *et al.* 2006), and the ongoing Dabbahu sequence (Hamling *et al.* 2009). The numerical models of Buck *et al.* (2006) show that the first event in the sequence cannot be treated in the same way as the subsequent events since it has by far the greatest length, width and duration. The required breakout pressure for the first dyke is ∼2.5 times larger than the subsequent dykes since the first intrusion may leave a hot, weak slot near the magma chamber that could aid formation of the later events. Thus, for our simple approach, we consider only the first dyke from each sequence.

4.1 Magma-driven dyke propagation model

Following the model of Segall *et al.* (2001), we consider a magma chamber connected via a conduit to a propagating dyke which takes the shape of a vertical, half-ellipsoidal penny-shaped crack. The model can be expressed as a system of four ordinary differential equations for the non-dimensionalized values of dyke length, $\tilde{a} = a/d$, dyke height $\tilde{b} = b/d$, chamber pressure $\tilde{p}_c = \Delta p_c/\Delta p_0$ and dyke pressure $\tilde{p}_d = \Delta p_d/\Delta p_0$, where d is depth to the base of the dyke and $\Delta\ p_0$ is the initial pressure.

The behaviour of the system is controlled by the lumped parameters R, α and ψ. In general, R relates to flow in the conduit, α relates to the driving overpressure and ψ relates to the magma chamber. More specifically, R is the ratio of characteristic time for dyke propagation to the characteristic time for magma flow in the conduit. α is the ratio of the effective head of a column of melt to the initial pressure within the dyke and Ψ is a measure of the compressibility and size of the magma chamber relative to the dyke. All equations are given in Segall *et al.* (2001). The system of equations can be solved numerically, and we use initial values of $\tilde{p}_d(0) = \tilde{p}_c(0) = 1$ and $\tilde{a}(0) = 2\tilde{b}(0) = 0.02$ as suggested by Segall *et al.* (2001).

Fig. 8 shows an example of the temporal evolution of dyke dimensions. Initially, the dyke grows fastest upwards before reaching its final depth and propagating lengthways. According to the model, the dyke will continue growing until the chamber pressure falls to zero. However, both the driving pressure difference $\tilde{p}_c - \tilde{p}_d$ and the rate of lateral propagation $\mathrm{d}\tilde{a}/\mathrm{d}t$ tend towards zero, such that thermal effects of freezing will restrict dyke growth (Fig. 9). For practical purposes, we assume dyke propagation essentially ends at time step 100. Observations suggest that a single dyke may be sourced by multiple magma chambers (Ebinger *et al.* 2008; Keir *et al.* 2009). However, since the chamber compressibility is independent of size (McTigue 1987), the equations of Segall *et al.* (2001) still apply, under the condition that V_c is the total volume of all the chambers.

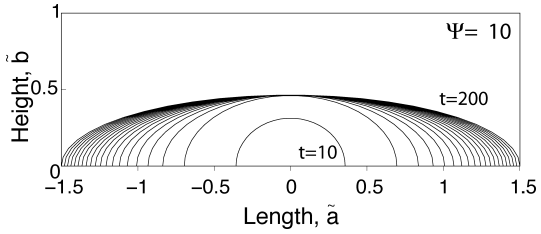

Figure 8. Time evolution of dyke dimensions plotted at intervals of 10 normalized time steps, after the model of Segall *et al.* (2001). Initially, the dyke grows fastest upwards before reaching its final depth and propagating lengthways.

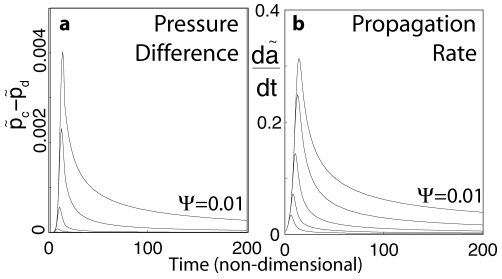

Figure 9. Evolution of driving pressure difference and rate of lateral propagation with time. As these factors decrease, thermal effects of cooling and increasing viscosity will restrict dyke growth. (a) Driving pressure difference between non-dimensionalized chamber pressure $\tilde{p}_c$ and dyke pressure $\tilde{p}_d$. The pressure difference drops rapidly after the initial phase of dyke propagation. (b) Rate of lateral dyke propagation $\mathrm{d}\tilde{a}/\mathrm{d}t$. The rate of propagation drops rapidly after the initial phase of growth, and unmodelled thermal effects will prevent propagation below a threshold value

We systematically vary all three lumped parameters and assess their influences on the final dyke dimensions. We find ψ, the parameter relating to the properties of the magma chamber, acts as the dominant control on dyke length. For $\psi \ll 1$ (corresponding to a large, shallow chamber), the chamber shows little pressure loss and acts as an infinite reservoir forming long, shallow dykes. For $\psi \gg 1$ (corresponding to a small, deep chamber), the chamber pressure drops rapidly favouring short, buried dykes. α primarily controls the dyke height, with little impact on dyke dimension (Figs 10c and d). The dyke length is weakly dependent on the parameter R, but since no observational constraints exist for the conduit dimensions in these examples, and few constraints exist in general, we chose not to over-interpret this possibility. We vary Ψ over five orders of magnitude from 0.01 to 100 (Figs 10a and b) and fix the values of $\alpha = 0.95$ and $R = 100$ such that the dyke does not break the surface, (i.e. $b < 1$).

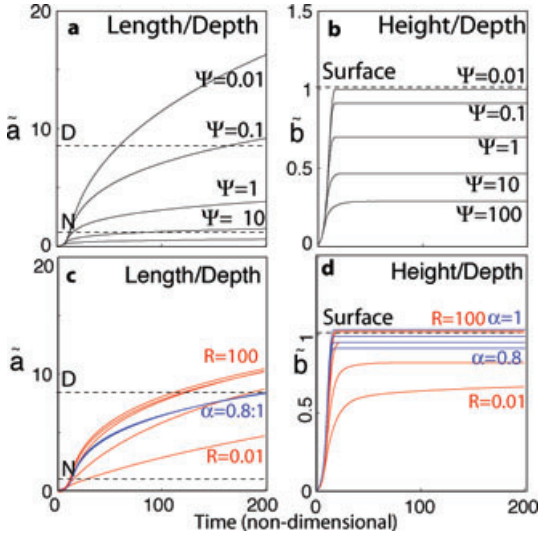

Figure 10. The effects of the lumped parameters Ψ, R and α on the dimensions of a propagating dyke. Non-dimensionalized dyke length, $\tilde{a}$; The Dabbahu Dyke had a non-dimensional length, $\tilde{a} \sim 8$ and the Lake Natron Dyke had a non-dimensional length $\tilde{a} \sim 1$. (b) Non-dimensionalized dyke height, $\tilde{b}$. When $\tilde{b} = 1$, the dyke reaches the surface and an eruption results.

4.1.1 Observations in the East African Rift Zone

We use InSAR-determined dyke lengths and a fixed base depth of 8 km to calculate length-to-depth ratios of 1 and 8 for Natron and Dabbahu respectively and use Fig. 10 to estimate the corresponding values of ψ to be 10 and 0.01. The parameter Ψ is inversely proportional to the chamber volume and directly proportional to the cube of the chamber depth. Hence, a decrease of ψ by a factor of 100 could be caused by an increase in chamber volume by a factor of 100, a decrease in chamber depth by a factor of 5, or a combination of both. The corresponding height-to-depth ratios (Fig. 10) indicate that the Dabbahu dyke came closer to the surface than the Natron dyke, consistent with observations of a small eruption (Wright *et al.* 2006). (*Note:* at height/depth = 1 the dyke touches the surface and erupts.)

Chamber size cannot be estimated from geodetic measurements alone so direct comparison is impossible for this parameter. The cavity radius and pressure change are linked and cannot be estimated independently (McTigue 1987) and calculations of volume change are complicated by the effects of gas exsolution and magma compressibility, often leading to a discrepancy in magma budgets (Rivalta & Segall 2008).

Our model calculations show that longer, shallower dykes, such as Dabbahu are favoured by large, shallow magma chambers, while shorter, buried dykes, such as Natron, are favoured by small, deep magma chambers. The crust in Afar is extending faster, and has greater cumulative extension resulting in thinner crust and a larger magma flux. Thermal considerations suggest the magma chamber would be larger and due to density effects shallower, consistent with our observations and modelling.

Similar relationships are predicted by the model of Buck *et al.* (2006), who found that the characteristic dyke length is inversely proportional to the pressure drop per unit volume of magma removed from the chamber, $\mathrm{d}P/\mathrm{d}V$. Since this is expected to be smaller for larger chambers, very large magma chambers could lead to very large dyke propagation distances.

Ideally, we would like to compare the differences in dyke width (8 m at Dabbahu; <2 m at Natron). However, unlike the dyke length and height, the width depends on magma pressure in the dyke so cannot be easily interpreted in a non-dimensionalized form. Similarly, to convert the non-dimensionalized time described here into physically meaningful quantities requires the use of parameters such as magma viscosity and compressibility. These parameters are poorly constrained and the errors associated with their inclusion would dominate the interpretation of the modelling results. Thus, we restrict our analysis to the simple non-dimensionalized system already described.

4.2 Thermal strain weakening

In terms of length, orientation and number of parallel strands, the difference between the Natron rifting episode and the Dabbahu rifting episode are analogous to those between earthquakes in immature and mature strike-slip systems, where the evolution of fault dimension and orientation is governed by frictional strain-weakening.

In the area of the Natron Dyke, the East African Rift comprises four distinct rifts with different orientations (Foster 1997) whereas in Afar, most of the plate opening is taken up on a single line of magmatic segments. Our observations show that the orientation of the Natron Dyke is oblique to the optimum direction but that the Dabbahu dyke is parallel to its optimum orientation. In Tanzania, intrusions with a range of orientations, probably on different strands,

are necessary to equal the overall plate motion, but in Afar, only a single active structure is required to accommodate the plate motion.

In strike-slip environments, the growth of fault gouge and loss of asperities with cumulative displacement favours fault simplification (Wesnousky 1988). In rifts, thermal effects appear to play a similar role in controlling the mechanical properties and behaviour of the crust. Conductive heating from magmatic underplating requires several million years to significantly weaken the crust, but once magma intrudes the middle-upper crust, advection-dominated heat transfer rapidly decreases crustal strength (Dixon *et al.* 1989). It may be useful to consider two types of strain weakening: 'thermal strain weakening' in magmatic systems and 'frictional strain weakening' in fault-controlled systems.

In Afar, repeated dyke intrusions have decreased crustal strength, forming a narrow weak zone along which dykes repeatedly intrude. In Tanzania, deformation occurs over a wider region and the precise location and orientation of the dyke is controlled by the local stress-field. We infer that dyke length in Afar is limited by the weakened magmatic segment rather than magma driving pressure. This is consistent with the observation of a continuing sequence of smaller dykes which have intruded into the axis of the 2005 Dabbahu dyke in the subsequent 2 yr (Hamling *et al.* 2009).

4.3 Importance of spreading rate

Investigation into the two case examples (Tanzania and Afar) have allowed us to formulate a hypothesis on dyke length, namely that the length of a dyke depends on magma chamber size and depth, which vary systematically according to spreading rate, magma flux and crustal thickness. This is a working hypothesis, designed to be tested by future observations.

The two events discussed here are the only dyke intrusions in the East African Rift system to be observed with modern satellite geodesy. However, field measurements and ground-based geodetic techniques provide information about other relevant events. Levelling and triangulation measurements of the 1978 Rifting episode in Asal-Ghoubbat, Djibouti are sparse and subsequent models have focussed primarily on rift perpendicular displacements (Cattin *et al.* 2005). Based on the figures of Ruegg *et al.* (1979), we estimate the dyke length to be on the order of 30 km.

Estimates of the length of the 1975 Krafla dyke are 70 km and 80 km for the 1875 Askja dyke (Tryggvason 1984). Comparisons with rifting episodes in Iceland are complicated by differences in tectonic setting—in particular, the presence of a hot spot influences the magma flux and crustal thickness. The rate of extension is slightly larger in Northern Iceland (20 mm yr^{-1}) than at Dabbahu, Afar (16 mm yr^{-1}) but the well-documented Krafla dyke intrusions bear many similarities to the sequence of events observed at Dabbahu. Both episodes consist of a multiyear sequence of discrete dyke intrusions (Buck *et al.* 2006; Hamling *et al.* 2009). In both cases, subsidence was observed associated with deflation of shallow magma chambers 2–4 km but subsequent analysis of the Dabbahu episode has indicated that a significant fraction of the magma was sourced from a deeper chamber (Keir *et al.* 2009).

Despite a limited number of examples, there appears to be a correlation between spreading rate and dyke length in rift settings (Fig. 11). Points from historical examples in Iceland, and Asal-Ghoubbet, Djibouti, fit well on a linear relationship based on the two recent examples at Natron, Tanzania and Dabbahu, Afar. Using the limited examples currently available, this plot suggests that spreading rate is the dominant control on dyke length along divergent plate boundaries, regardless of differences in crustal thickness and magma flux. In combination with the previous section, this implies that spreading rate is the fundamental control on magma chamber depth and size.

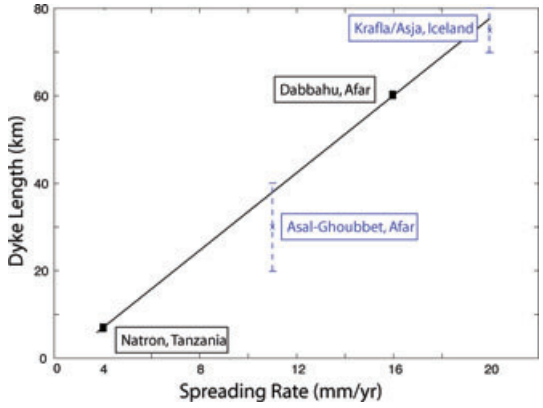

Figure 11. Empirical relationship between dyke length and spreading rate for subaerial extensional settings. Black squares are recent events in the East African Rift observed using InSAR. Blue bars represent events from other tectonic settings (Iceland) and using surveying techniques (Asal-Ghoubbet).

5 CONCLUSION

We present geodetic observations of the evolution of a rifting episode in an immature continental rift. The earliest major surface displacements were caused by a normal-faulting earthquake; shallow dyke intrusion began 3 d into the seismic swarm and a shallow graben collapsed 2 d later. The observations support a conceptual model in which the dyke propagates laterally in a period of hours and then inflates widthwise for days to weeks.

Dyke propagation models show dyke length is strongly influenced by magma chamber size and depth. Longer, shallower dykes are favoured by large, shallow magma chambers, while shorter, buried dykes are favoured by small, deep magma chambers. The order-of-magnitude difference in length between the 2005 Dabbahu dyke (Afar) and the Natron Dyke (Tanzania) can be attributed to a shallower, larger magma chamber consistent with a thinner crust and higher magma flux, in turn related to spreading rate.

ACKNOWLEDGMENTS

JB was supported by the Rosenstiel Postdoctoral Fellowship from the University of Miami, CSTARS and a Lindemann Fellowship from the English Speaking Union. NG was supported by the NASA Earth System Science fellowship. Data were provided by ASF, JAXA and ESA (Cat 1361). This paper benefited greatly from constructive reviews from Pall Einarsson, San-Ho Yun and one anonymous reviewer and from useful discussions with Cindy Ebinger and Tim Wright. This is CSTARS contribution number 19.

REFERENCES

Aoki, Y., Segall, P., Kato, T., Cervelli, P. & Shimada, S., 1999. Imaging magma transport during the 1997 seismic swarm off the Izu Peninsula, Japan, *Science,* **286,** 927–930.

Ayele, A. *et al.*, 2007. The volcano seismic crisis in Afar, Ethiopia, starting September 2005, *Earth planet. Sci. Lett.,* **255,** 177–187.

Baer, G., Hamiel, Y., Shamir, G. & Nof, R., 2008. Evolution of a magma-driven earthquake swarm and triggering of the nearby Oldoinyo Lengai eruption, as resolved by InSAR, ground observations and elastic modeling, East African Rift, 2007, *Earth planet. Sci. Lett.,* **272,** 339–352, doi:10.1016/j.epsl.2008.04.052.

Bechor, N.B.D. & Zebker, H.A., 2006. Measuring two-dimensional movements using a single InSAR pair, *Geophys. Res. Lett.,* **33,** 16311, doi:10.1029/2006GL026883.

Buck, W.R., Einarsson, P. & Brandsdóttir, B., 2006. Tectonic stress and magma chamber size as controls on dike propagation: constraints from the 1975–1984 Krafla rifting episode, *J. geophys. Res. (Solid Earth),* **111,** B12404, doi:10.1029/2005JB003879.

Calais, E. *et al.*, 2008. Strain accommodation by slow slip and dyking in a youthful continental rift, East Africa, *Nature,* **456,** 783–787.

Cattin, R., Doubre, C., de Chabalier, J.-B., King, G., Vigny, C., Avouac, J.-P. & Ruegg, J.-C., 2005. Numerical modelling of quaternary deformation and post-rifting displacement in the Asal-Ghoubbet rift (Djibouti, Africa) [rapid communication], *Earth planet. Sci. Lett.,* **239,** 352–367.

Cervelli, P., Segall, P., Amelung, F., Garbeil, H., Meertens, C., Owen, S., Miklius, A. & Lisowski, M., 2002. The 12 September 1999 Upper East Rift Zone dike intrusion at Kilauea Volcano, Hawaii, *J. geophys. Res.,* **107**(B7), 2150, doi:10.1029/2001JB000602.

Dawson, J., Keller, J. & Nyamwenu, C., 1995. Historic and recent eruptive activity of Oldoinyo Lengai, in *Carbonatite Volcanism: Oldoinyo Lengai and the Petreogensesis of Natrocarbonatites,* pp. 4–22, eds Bell, K. & Keller, J., IAVCEI Proc. in Volcanology, Springer, Berlin.

Dawson, J.B., Bowden, P. & Clark, G.C., 1968. Activity of the carbonatite volcano Oldoinyo Lengai, 1966, *Geologische Rundschau,* **57,** 865–879.

Dawson, J.B., Pinkerton, H., Pyle, D.M. & Nyamweru, C., 1994. June 1993 eruption of Oldoinyo Lengai, Tanzania: exceptionally viscous and large carbonatite lava flows and evidence for coexisting silicate and carbonate magmas, *Geology,* **22,** 799–802.

Dixon, T.H., Ivins, E.R. & Franklin, B.J., 1989. Topographic and volcanic asymmetry around the Red Sea—constraints on rift models, *Tectonics,* **8,** 1193–1216.

Dziak, R.P., Fox, C.G. & Schreiner, A.E., 1995. The June–July 1993 seismo-acoustic event at CoAxial segment, Juan de Fuca Ridge: evidence for a lateral dike injection, *Geophys. Res. Lett.,* **22,** 135–138.

Dziewonski, A. & Anderson, D., 1981. Preliminary Reference Earth Model, *Phys. Earth planet. Inter.,* **25,** 297–356.

Ebinger, C. *et al.*, 2008. Capturing magma intrusion and faulting processes during continental rupture: seismicity of the Dabbahu (Afar) rift, *Geophys. J. Int.,* **174,** 1138–1152.

Ebinger, C.J., 2005. Continental break-up: the East African perspective, *Astron. Geophys.,* **46,** 2.16–2.21.

Ebinger, C.J. & Casey, M., 2001. Continental breakup in magmatic provinces: an Ethiopian example, *Geology,* **29,** 527–+.

Foster, A., 1997. Tectonic development of the northern Tanzanian sector of the East African Rift System, *J. geol. Soc. Lond.,* **154,** 689–700.

Goldstein, R., Zebker, H. & Werner, C., 1988. Satellite radar interferometry: two dimensional phase unwrapping, *Radio Sci.,* **23**(4), 713–720.

Hamling, I., Ayele, A., Calais, E., Ebinger, C., Keir, D., Lewi, E., Wright, T. & Yirgu, G., 2009. Geodetic observations of new dyke intrusions in the Dabbahu rift segment, Afar, Ethiopia, *Geophys. J. Int.,* **178,** 989–1003.

Hauksson, E., 1983. Episodic rifting and volcanism at Krafla in North Iceland—growth of large ground fissures along the plate boundary, *J. geophys. Res.,* **88,** 625–636.

Jonsson, S., Zebker, H., Segall, P. & Amelung, F., 2002. Fault slip distribution of the M_w 7.2 Hector Mine earthquake estimated from satellite radar and GPS measurements, *Bull. seism. Soc. Am.,* **92,** 1377–1389.

Jung, H.-S., Won, J.-S. & S.-W., K., 2009. An improvement of the performance of multiple aperture SAR interferometry (MAI), *IEEE Trans. Geosci. Remote Sens.,* in press.

Kanamori, H., 1977. The energy release in great earthquakes, *J. geophys. Res.,* **82**(20), 2981–2987.

Keir, D. et al., 2009. Evidence for focused magmatic accretion at segment centers from lateral dike injections captured beneath the Red Sea rift in Afar, *Geology,* **37,** 59–62.

Kervyn, F., Mattsson, H., Belton, F., Mbede, E. & Jacobs, P., 2008. Voluminous lava flows at Oldoinyo Lengai in 2006: chronology of events and insights into the shallow magmatic system, *Bull. Volcanol.,* **70,** 1069–1086.

Manga, M. & Brodsky, E., 2006. Seismic triggering of eruptions in the far field: volcanoes and geysers, *Ann. Rev. Earth planet. Sci.,* **34,** 263–291.

McTigue, D.F., 1987. Elastic stress and deformation near a finite spherical magma body: resolution of the point source paradox, *J. geophys. Res.,* **92,** 12 931–12 940.

Mogi, K., 1958. Relations between eruptions of various volcanoes and the deformations of the ground surfaces around them, *Bull. Earthq. Res. Inst.,* **36,** 99–134.

Nyamweru, C., 1990. Observations on changes in the active crater of Ol Doinyo Lengai from 1960 to 1988, *J. Afric. Earth Sci.,* **11,** 385–390.

Nyamweru, C., 1997. Changes in the crater of Oldoinyo Lengai: June 1993 February 1997, *J. Afric. Earth Sci.,* **25,** 43–53.

Okada, Y., 1985. Surface deformation due to shear and tensile faults in a half-space, *Bull. seism. Soc. Am.,* **75,** 1135–1154.

Rivalta, E. & Segall, P., 2008. Magma compressibility and the missing source for some dike intrusions, *Geophys. Res. Lett.,* **35,** 4306, doi:10.1029/2007GL032521.

Rosen, P., Hensley, S., Peltzer, G. & Simons, M., 2004. Updated Repeat Orbit Interferometry package released, *EOS, Trans. AGU,* **85**(5), doi:10.1029/2004EO050004.

Rowland, J.V., Baker, E., Ebinger, C.J., Keir, D., Kidane, T., Biggs, J., Hayward, N. & Wright, T.J., 2007. Fault growth at a nascent slow-spreading ridge: 2005 Dabbahu rifting episode, Afar, *Geophys. J. Int.,* **171,** 1226–1246.

Rubin, A.M., 1992. Dike-induced faulting and graben subsidence in volcanic rift zones, *J. geophys. Res.,* **97,** 1839–1858.

Rubin, A.M., 1995. Propagation of magma-filled cracks, *Ann. Rev. Earth planet. Sci.,* **23,** 287–336.

Ruegg, J., Lpine, J., Tarantola, A. & Kasser, M., 1979. Geodetic measurements of rifting associated with a seismo-volcanic crisis in Afar, *Geophys. Res. Lett.,* **6**(11), 817–820.

Scordilis, E.M., 2006. Empirical global relations converting M_S and m_b to moment magnitude, *J. Seismol.,* **10,** 225–236.

Segall, P., Cervelli, P., Owen, S., Lisowski, M. & Miklius, A., 2001. Constraints on dike propagation from continuous GPS measurements, *J. geophys. Res.,* **106,** 19 301–19 318.

Sella, G.F., Dixon, T.H. & Mao, A., 2002. REVEL: a model for recent plate velocities from space geodesy, *J. geophys. Res.,* **107**(B4), doi:10.1029/2000JB000033.

Stamps, D.S., Calais, E., Saria, E., Hartnady, C., Nocquet, J.-M., Ebinger, C.J. & Fernandes, R.M., 2008. A kinematic model for the East African Rift, *Geophys. Res. Lett.,* **35,** 5304, doi:10.1029/2007GL032781.

Tryggvason, E., 1984. Widening of the Krafla fissure swarm during the 1975 1981 volcano-tectonic episode, *Bull. Volcanol.,* **47,** 47–69.

Vaughan, R., Kervyn, M., Realmuto, V., Abrams, M. & Hook, S., 2008. Satellite measurements of recent volcanic activity at Oldoinyo Lengai, Tanzania, *J. Volc. Geotherm. Res.,* **173,** 196–206.

Walter, T. & Amelung, F., 2007. Volcanic eruptions following M 9 megathrust earthquakes: implications for the Sumatra-Andaman volcanoes, *Geology,* **35,** 539–542.

Wesnousky, S.G., 1988. Seismological and structural evolution of strike-slip faults, *Nature,* **335,** 340–343.

Wright, T., Ebinger, C., Biggs, J., Ayele, A., Yirgu, G., Keir, D. & Stork, A., 2006. Magma-maintained rift segmentation at continental rupture in the 2005 Afar dyking episode, *Nature,* **442,** 291–294.